Industrial Chemistry & Materials

ROYAL SOCIETY OF CHEMISTRY

PAPER

View Article Online
View Journal



Cite this: DOI: 10.1039/d6im00077k

# Bioinspired Fe/Ni bimetallic species on carbonized MOF as bifunctional electrocatalysts for rechargeable Zn–air batteries

Sunggu Park, †[a] Hung Ngo Manh,†[b] Seyeop Jeong,†[a] Heesun Kim,[a] Jun Ho Seok,[b] Seokhyeon Jeon,[a] Yunseok Shin,[a] Ali Anus,[a] Sang Uck Lee *[b] and Sungjin Park *[a]

A bioinspired bimetallic single-atom-based catalyst (Fe/Ni-NC) is generated on N-doped porous carbon derived from ZIF-8 for rechargeable zinc–air batteries (ZABs). Fe and Ni atoms are sequentially introduced into the support networks and stabilized through high-temperature pyrolysis, yielding atomically dispersed Fe–N and Ni–N sites without forming metal nanoparticles. Comprehensive structural characterization confirms the atomic dispersion of Fe and Ni within the carbon matrix. Electrochemical evaluations reveal that Fe/Ni-NC exhibits superior bifunctional oxygen reduction reaction (ORR) and oxygen evolution reaction (OER) performance with a low Tafel slope, excellent selectivity for a four-electron ORR pathway, and minimal charge transfer resistance. Density functional theory (DFT) analysis reveals that Ni sites embedded within pyrrolic-N environments (Ni@mPrN) possess optimal O* adsorption energies, serving as the dominant bifunctional active centers responsible for the enhanced oxygen reduction and evolution activities. In ZABs, the catalyst delivers a high open-circuit voltage (1.55 V), peak power density (130.9 mW $cm^{-2}$), and specific capacity (775 mAh $g_{Zn}^{-1}$), along with outstanding electrochemical durability. This study highlights the synergistic effect of dual single-atom-based species and porous N-doped carbon in enabling cost-effective, high-performance air cathodes for ZABs.

Keywords: Zinc–air batteries; Single-atom catalysts; Bimetallic catalysts; Oxygen reduction reaction; Oxygen evolution reaction; Electrocatalysts.

Received 28th February 2026,
Accepted 3rd June 2026

DOI: 10.1039/d6im00077k

rsc.li/icm



## 1 Introduction

Rechargeable metal–air batteries have attracted attention as promising sustainable energy storage systems. Because they have an open-cell structure, external oxygen molecules can be supplied to the cathode continuously, generating higher theoretical energy densities than lithium-ion batteries.[1,2] Among them, zinc–air batteries (ZABs) stand out as promising candidates because of their environmental friendliness, cost-effectiveness, and safety.[3,4] However, the sluggish kinetics of the oxygen reduction reaction (ORR) and oxygen evolution reaction (OER) at the air electrode significantly limit the practical usage of ZABs. Therefore, the development of highly active and durable bifunctional electrocatalysts working for the ORR and OER is crucial for the industrial application of ZABs.[5]

It is well-known that precious metal-based materials such as Pt/C and $IrO_2/RuO_2$ show outstanding electrocatalytic performance for the ORR and OER in separate half-cell conditions, respectively.[6–8] Thus, combining such ORR and OER active species into one electrode has been widely studied as bifunctional electrocatalysts for ZABs.[9] However, because of their limitations of high cost, scarcity, and low long-term stability, recent research has focused on developing alternative non-precious metal-based catalysts.[10] Although earth-abundant metal species such as Co, Fe, and Ni show the possibility of being bifunctional electrocatalysts, achieving high ZAB performance and stability is still a great challenge.[11–13] Engineering highly active species for both the ORR and OER is a key factor to address such issues.[14,15] Nature systems such as hydrogenase often rely on bimetallic catalytic systems, including Fe and Ni, to facilitate energy conversion processes in aqueous environments with remarkable selectivity and efficiency.[16] Therefore, inspired by the efficient catalytic systems found in nature (enzymatic

[a] Department of Chemistry and Chemical Engineering, Inha University, 100 Inha-ro, Michuhol-gu, Incheon 22212, Republic of Korea. E-mail: sungjinpark@inha.ac.kr
[b] School of Chemical Engineering, Sungkyunkwan University, Suwon 16419, Republic of Korea. E-mail: suleechem@skku.edu
† These authors contributed equally to this work.

reactions and biological processes), we propose a bioinspired strategy for artificial bimetallic electrocatalysts.[17]

Recent studies have demonstrated that Fe/Ni-based bimetallic single-atom catalysts (SACs) in carbon-based frameworks exhibit excellent electrocatalytic activity toward the ORR and OER.[18–20] Owing to their tunable electronic environments, large surface areas, high electrical conductivity, and robust chemical stability, carbon-based materials have emerged as promising supporting networks for both electro- and photocatalytic SACs. Such SACs on the surfaces of support offer maximized atomic utilization and unique electronic structures that promote reaction kinetics.[21,22] However, achieving commercially viable ZAB devices using bifunctional bimetallic catalysts as air-electrode electrocatalysts remains a critical challenge, requiring the development of highly efficient catalysts as well as the realization of high-performance, high-efficiency, and long-term stable ZAB operation. Furthermore, the enhanced catalytic performance of Fe/Ni-based bimetallic systems has generally been attributed to the synergistic effects arising from the coexistence of Fe and Ni species, including charge redistribution, modulation of the electronic structure, and optimization of oxygen intermediate adsorption energies, all of which contribute to improved ORR/OER activity.[23–25] Nevertheless, precise control over the structure of SAC active sites typically formed at defect sites on $sp^2$-carbon supports along with a deeper understanding of the active species and the development of optimal synthetic strategies for incorporating heterometallic centers are still required.

Metal–organic frameworks (MOFs) have emerged as a versatile platform as support materials for designing advanced electrocatalysts due to their porosity, high surface area, and ability to accommodate atomically dispersed metal active sites.[21,22] Herein, we report the synthesis of a novel bimetallic catalyst (Fe/Ni-NC) in which atomically dispersed active species are anchored on the surface of an N-doped MOF-derived carbonaceous structure. The morphological and chemical structures were thoroughly investigated. Fe/Ni-NC materials show excellent bifunctional electrocatalytic activity for the ORR and OER separately. Additionally, combined experimental analyses and density functional theory (DFT) calculations provide atomic-level insight into how Fe and Ni atoms embedded within distinct nitrogen coordination environments modulate oxygen electrocatalysis, thereby identifying the dominant active configurations responsible for the enhanced ORR and OER activities. Furthermore, the Fe/Ni-NC air electrode exhibits superior ZAB performance in terms of power density, cycle stability, and overall energy efficiency.

## 2 Results and discussion

### 2.1 Preparation and morphological characterization of Fe/Ni-NC

In this study, zeolitic imidazolate framework (ZIF)-8, a subclass of MOF, was employed as an initial template for the synthesis of porous carbon materials owing to its facile preparation and low cost.[26] ZIF-8 was synthesized *via* a solution-phase reaction between zinc nitrate hexahydrate ($Zn(NO_3)_2{\cdot}6H_2O$) and 2-methylimidazole ($C_4H_6N_2$) in methanol (Fig. 1). The obtained ZIF-8 powder was subsequently carbonized at 950 °C under a nitrogen atmosphere, yielding N-doped porous carbon (NC) materials. To introduce the atomic Fe and Ni species, the NC powder was sequentially treated with $FeCl_2{\cdot}4H_2O$ and $NiCl_2{\cdot}6H_2O$ in ethylene glycol (EG), which acts as a mild reducing agent as well as a solvent. The resulting mixture was subjected to thermal annealing at 900 °C under a $N_2$ atmosphere to produce the bimetallic SAC, denoted as Fe/Ni-NC. For comparison, monometallic control samples (Fe-NC and Ni-NC) and a bimetallic sample with simultaneous addition (FeNi-NC) were also prepared as controls.

The morphological and structural features of Fe/Ni-NC were investigated using X-ray diffraction (XRD), transmission electron microscopy (TEM), and Brunauer–Emmett–Teller (BET) surface area analysis. The XRD patterns of both NC and Fe/Ni-NC exhibit a broad diffraction peak centered at approximately 25°, which corresponds to the (002) plane of graphitic carbon, indicating the presence of amorphous $sp^2$-hybridized carbon layers (Fig. 2a).[25,27] This is in sharp contrast to the well-defined crystalline peaks observed in the pristine ZIF-8 structure (Fig. S1), confirming the successful carbonization and transformation into an amorphous carbon matrix during thermal treatment.

Notably, no distinct peaks corresponding to crystalline Fe- or Ni-containing phases are detected in the XRD patterns of Ni-NC, Fe-NC and Fe/Ni-NC (Fig. S2). This feature suggests that the Fe and Ni species could be atomically dispersed.[28] In contrast, the XRD pattern of the control FeNi-NC sample (synthesized *via* simultaneous introduction of Fe and Ni precursors) exhibits sharp peaks that can be assigned to $Fe_2O_3$ and/or spinel-type $Fe_{1.85}Ni_{1.25}O_4$ phases, indicating the formation of crystalline nanoparticles (Fig. 2a). This difference clearly demonstrates that the sequential metal incorporation strategy in this work is essential for preventing nanoparticle formation and achieving atomically dispersed Fe and Ni sites on the surfaces of carbon-based supports (the local environments of the metal centers will be discussed later).

TEM images of the ZIF-8 particles show well-defined polyhedral morphologies (Fig. S3). After pyrolysis and metal incorporation, the Fe/Ni-NC sample retains a similar polygonal shape to NC with slight shrinkage, and the particles appear amorphous (Fig. S4 and 2b). The particle sizes range from 160 to 200 nm, with an average diameter of approximately 168 nm (Fig. 2b). In addition, Ni-NC and Fe-NC also show morphologies comparable to that of Fe/Ni-NC (Fig. S5 and S6). To further investigate the sample, High-Angle Annular Dark-Field Scanning Transmission Electron Microscopy (HAADF-STEM) measurements along with elemental mapping were carried out on Fe/Ni-NC (Fig. 2c and d). Elemental mapping images confirm a uniform distribution of Fe and Ni throughout the carbon matrix, alongside a dominant carbon framework. High-resolution

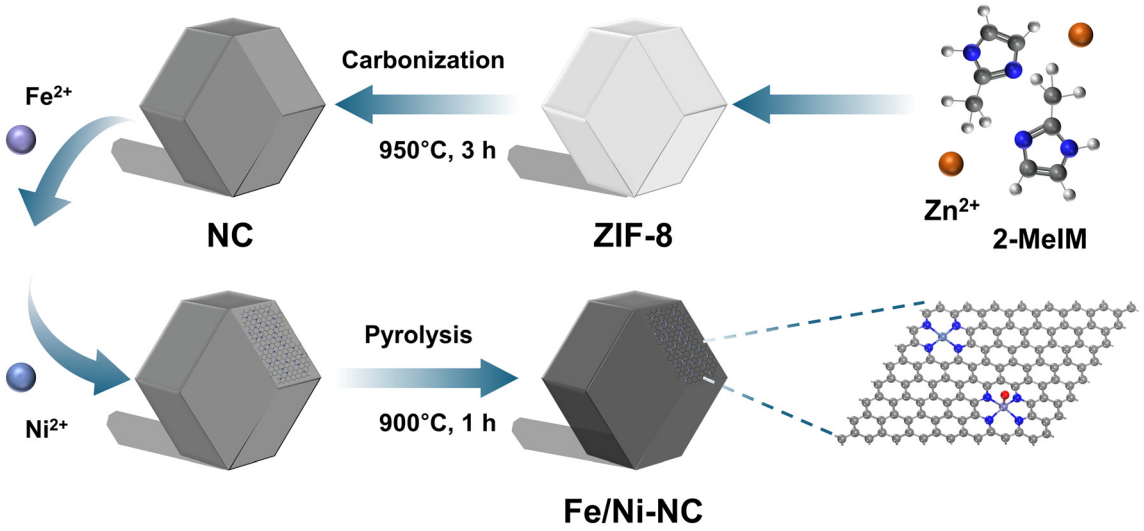


**Fig. 1** Scheme for preparing Fe/Ni-NC.

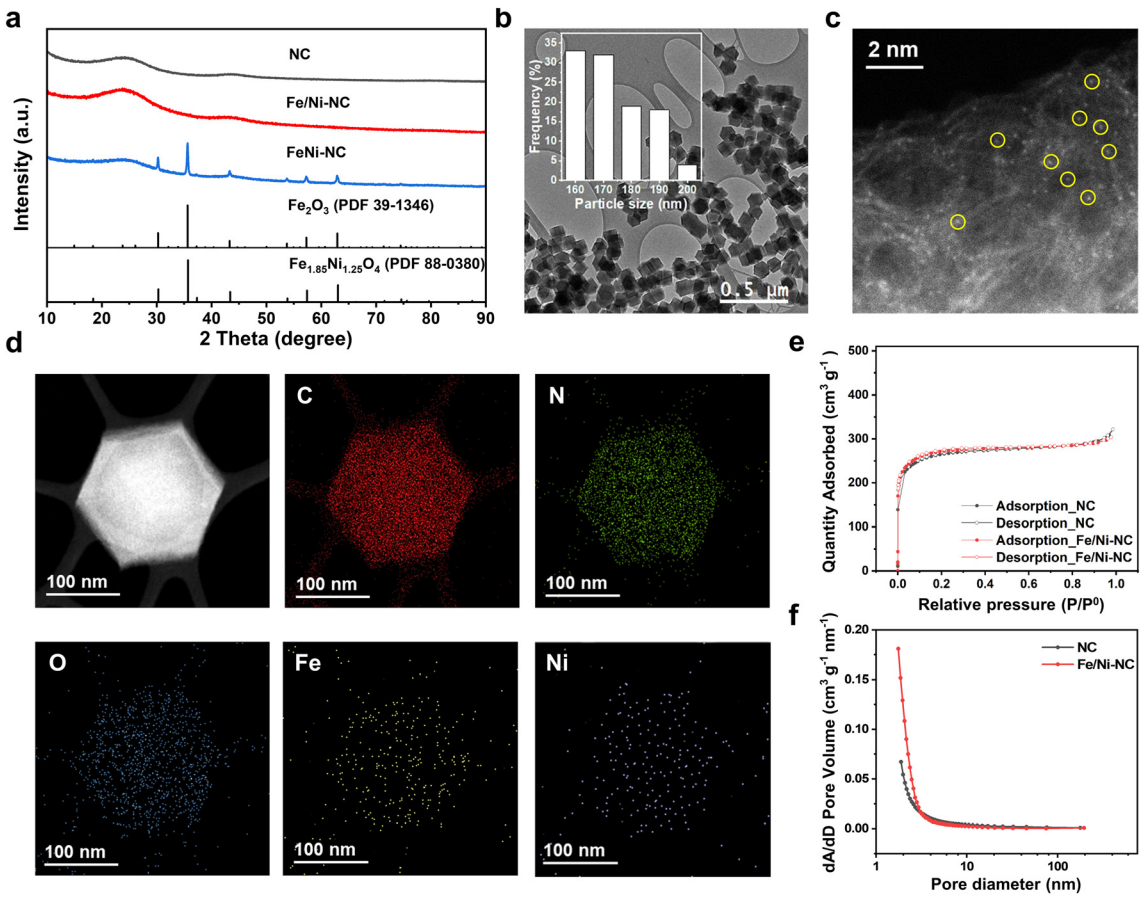


**Fig. 2** (a) XRD patterns of NC, Fe/Ni-NC, FeNi-NC and references; (b) TEM image of Fe/Ni-NC with the corresponding particle size distribution shown in the inset; (c) HAADF-STEM image of Fe/Ni-NC; (d) STEM and elemental mapping images of Fe/Ni-NC; (e) $N_2$ adsorption/desorption isotherm curves and (f) pore size distribution of NC and Fe/Ni-NC.

imaging as shown in Fig. 2c and S7 clearly demonstrates the uniform dispersion of metal species at a scale below 1 nm (denoted by the circles), confirming the absence of aggregated metallic nanoparticles within the carbon matrix. Overall, these findings provide strong evidence for the uniform dispersion of the Fe and Ni species at the sub-nanometer

scale, with no detectable formation of crystalline phases. Furthermore, the specific metal loadings were quantified as 1.20 wt% for Fe and 1.09 wt% for Ni through inductively coupled plasma-optical emission spectrometry (ICP-OES) analysis. Raman spectroscopy further supports the formation of carbon-based structures from ZIF-8, showing characteristic D and G bands, which correspond to disordered carbon and graphitic $sp^2$ domains,[29] respectively (Fig. S8 and S9).

The Fe/Ni-NC sample exhibits a high Brunauer–Emmett–Teller (BET) surface area of 1036 $m^2\ g^{-1}$, which is slightly higher than that of the NC sample (960 $m^2\ g^{-1}$). All samples display isotherms that are a combination of type I and type IV, according to the IUPAC classification,[30] suggesting the coexistence of microporous and mesoporous structures (Fig. 2e and S10). The sharp uptake of $N_2$ at low relative pressures ($P/P_0 < 0.1$) indicates the predominant presence of micropores. A more gradual increase in adsorption in the intermediate $P/P_0$ region reflects the presence of mesopores. In addition, the steep rise in $N_2$ uptake at high $P/P_0$ values ($P/P_0 > 0.9$) can be ascribed to interparticle voids or textural porosity resulting from loosely packed carbon particles.[31] The Barrett–Joyner–Halenda (BJH) pore size distribution curves further support the microporosity of both NC and Fe/Ni-NC, with a minor contribution from mesopores (Fig. 2f). Fe/Ni-NC shows a slightly higher micropore volume compared to NC, indicating that the incorporation of metal species through the sequential coordination and heat treatment process does not compromise the microporosity of the carbon framework.[32] This porosity and high surface area are advantageous for catalytic applications, as they can facilitate effective dispersion of active sites and improve the mass transport of reactants and products during electrochemical reactions.

### 2.2 Chemical analyses of Fe/Ni-NC

The structural and electronic characteristics of Fe/Ni-NC were investigated by X-ray photoelectron spectroscopy (XPS), X-ray absorption near edge structure (XANES), and extended X-ray absorption fine structure (EXAFS) analyses. As summarized in Table S1, XPS survey spectra reveal that Fe/Ni-NC is primarily composed of C atoms, with minor contributions from N and O atoms. Compared to the pristine NC sample, Fe/Ni-NC exhibits lower oxygen content, indicating the removal of oxygen-containing moieties during the high-temperature pyrolysis process.[33]

The C 1s XPS spectrum of NC (Fig. 3a) displays a dominant peak at 284.6 eV, corresponding to C=C bonds, which is indicative of the formation of $sp^2$-hybridized graphitic carbon derived from the thermal decomposition of the ZIF-8 framework. Additional peaks associated with oxygenated and N-containing functional groups are also observed.[34] The N 1s spectrum (Fig. 3b) is deconvoluted into multiple components, with peaks located at 398.4, 400.8, 402.3, and 403.0 eV, assignable to pyridinic, pyrrolic, graphitic, and oxidized N species, respectively.[35,36] These results confirm the successful incorporation of N atoms into the carbon lattice, forming an N-rich environment capable of stabilizing metal active sites. Nitrogen functionalities are known to serve as Lewis base sites that can coordinate transition metal species, forming metal–N ($M–N_x$) coordination structures.[37] In the case of Fe/Ni-NC, a similar N configuration is retained, along with an additional peak

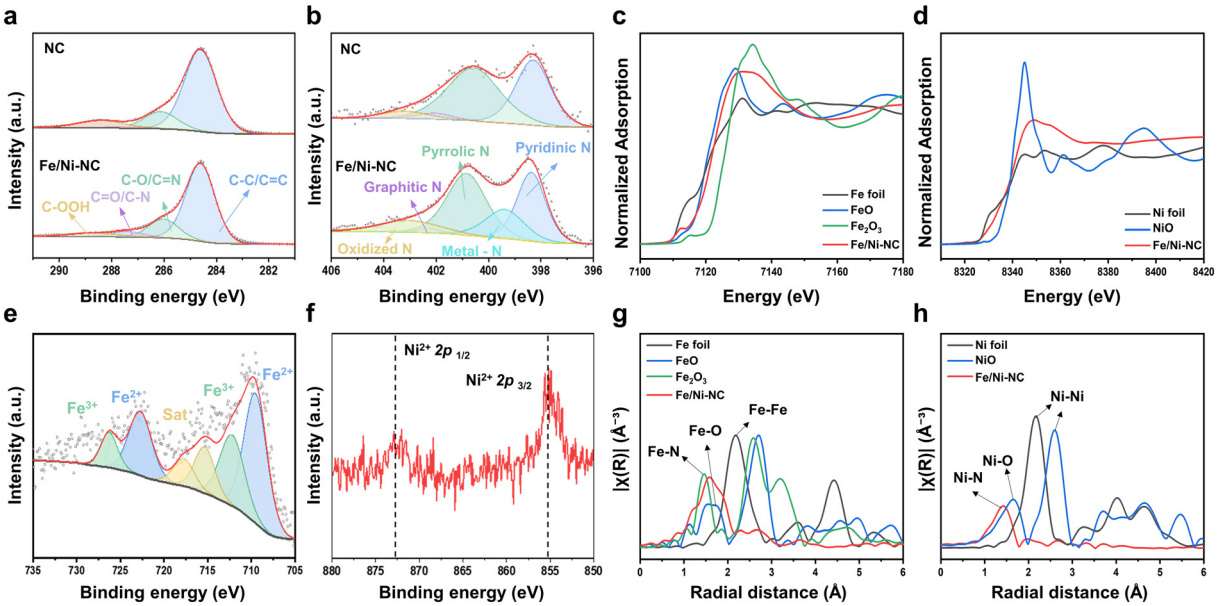


**Fig. 3** Deconvoluted XPS spectra of NC and Fe/Ni-NC for (a) C 1s and (b) N 1s; (c) Fe K-edge XANES spectra of Fe foil, FeO, $Fe_2O_3$, and Fe/Ni-NC; (d) Ni K-edge XANES spectra of Ni foil, NiO, and Fe/Ni-NC; deconvoluted XPS spectra of Fe/Ni-NC for (e) Fe 2p and (f) Ni 2p; (g) EXAFS fitting spectra in the *R*-space for Fe foil, FeO, $Fe_2O_3$, and Fe/Ni-NC; (h) EXAFS fitting spectra in the *R*-space for Ni foil, NiO, and Fe/Ni-NC.

attributed to M–N coordination bonds. Notably, the pyrrolic N peak shifts slightly toward higher binding energy (from 400.6 eV in NC to 400.8 eV in Fe/Ni-NC), suggesting an electronic interaction between pyrrolic N moieties and Ni centers. Such shifts have been reported as characteristic signatures of pyrrolic Ni–N coordination, indicating that pyrrolic N species are likely to contribute to anchoring Ni single atoms in the Fe/Ni-NC structure.[38] This supports the presence of Fe and Ni centers anchored to N sites of the carbon matrix. All these features suggest the formation of Fe–N and Ni–N motifs, which are considered catalytically active centers for electrocatalysis. For comparison, the corresponding XPS spectra of the control samples are provided in the SI (Fig. S11).

Further insights into the local coordination environment and oxidation states of Fe and Ni are obtained from X-ray absorption near-edge structure (XANES) and extended X-ray absorption fine structure (EXAFS) analyses. Fig. 3c and d present the Fe and Ni K-edge XANES spectra of Fe/Ni-NC, along with those of reference samples. The electronic transitions from 1s → 3d and 1s → 4p are manifested as characteristic pre-edge and white-line features, respectively.[39] The absorption profiles of Fe and Ni in the Fe/Ni-NC catalyst exhibit a significant deviation from those of the metallic Fe and Ni foils, providing clear evidence that both metal species exist in non-metallic states. For Fe, the XANES profile is similar to that of FeO, though the broader white-line peak lies intermediate between those of FeO and $Fe_2O_3$. This feature suggests that an average Fe oxidation state is slightly higher than +2. In the case of Ni, the XANES feature closely matches that of NiO, indicating that Ni is predominantly in the oxidation state of +2.

These XANES findings are consistent with the XPS results. The Fe 2p XPS spectrum (Fig. 3e) of Fe/Ni-NC shows peaks at 709.5 eV and 722.9 eV, attributed to $Fe^{2+}$ $2p_{3/2}$ and $2p_{1/2}$, respectively, along with minor features at 712.2 eV and 726.1 eV corresponding to $Fe^{3+}$ species.[40] The Ni 2p spectrum (Fig. 3f) exhibits peaks at 856.3 eV and 873.9 eV, corresponding to $Ni^{2+}$ $2p_{3/2}$ and $2p_{1/2}$, further supporting the presence of $Ni^{2+}$ species in Fe/Ni-NC.[41]

To elucidate the local coordination environment of the metal atoms, EXAFS analysis was performed. The *k*-space oscillations and Fourier-transformed (*R*-space) EXAFS spectra for the Fe and Ni K-edges (Fig. 3g and h) were compared with those of metallic and oxide references. As summarized in Table S2, no significant peaks corresponding to Fe–Fe or Ni–Ni metallic bond distances are observed in the Fe/Ni-NC spectra, indicating the absence of metal nanoparticles in Fe/Ni-NC.

In the Fe EXAFS spectrum, signals corresponding to Fe–O and Fe–Fe interactions, typically observed in iron oxides (*e.g.*, at 2.13 and 1.99 Å for FeO and $Fe_2O_3$), are absent in Fe/Ni-NC. Instead, a distinct peak is observed at 2.03 Å, which can be fitted to a Fe–N scattering path, indicative of Fe–N coordination.[42] A similar trend is found in the Ni EXAFS spectrum, where NiO shows the features arising from Ni–O and Ni–Ni distances, and the Fe/Ni-NC sample shows a single peak corresponding to a Ni–N path.[43] As mentioned earlier, the presence of M–N coordination is further supported by the N 1s XPS spectrum of Fe/Ni-NC, which exhibits a corresponding peak at 399.4 eV. EXAFS fitting results indicate that the coordination numbers for Fe–N and Ni–N are 3.62 and 3.80, respectively (Table S2), indicating different coordination environments from those of bulk oxides or metallic phases. Collectively, the XPS and XANES results indicate that the Fe and Ni species are in positively charged states, while EXAFS analysis shows that these metal centers are coordinated to N atoms in isolated M–$N_x$ configurations. These features combined with STEM data provide strong evidence that Fe and Ni are atomically dispersed within the N-doped carbon matrix, rather than existing as aggregated nanoparticles or metal oxide clusters.[18]

### 2.3 Rechargeable Zn–air battery performance

To evaluate the rechargeable ZAB performance of the synthesized Fe/Ni-NC catalyst, battery cells were assembled in a custom configuration (Fig. S12). The cell consisted of a Zn plate anode, an air cathode based on a gas diffusion layer coated with Fe/Ni-NC, and an aqueous electrolyte containing 6.0 M KOH and 0.2 M $Zn(CH_3COO)_2$. For comparison, a reference cell employing a commercial Pt/C and $RuO_2$ mixture (1 : 1, w/w) was prepared under identical conditions. The Fe/Ni-NC-based ZABs exhibit an open-circuit voltage (OCV) of 1.55 V, surpassing the Pt/C + $RuO_2$ cell (1.47 V) (Fig. 4a). This higher OCV is indicative of electrochemically effective surfaces and morphology of Fe/Ni-NC relative to Pt/C + $RuO_2$ in three-phase interfaces. The discharge polarization and power density profiles (Fig. 4b) reveal that the Fe/Ni-NC-based ZABs produce a significantly higher current density of 239.7 mA $cm^{-2}$ at 0.5 V, compared to the Pt/C + $RuO_2$ system (205.7 mA $cm^{-2}$). Furthermore, it achieves a peak power density of 130.9 mW $cm^{-2}$, outperforming the noble-metal-based counterpart (107.3 mW $cm^{-2}$), which shows the outstanding bifunctional catalytic activity of Fe/Ni-NC.

In the full-discharge test conducted at a constant current density of 10 mA $cm^{-2}$ (Fig. 4c), the Fe/Ni-NC-based ZABs reach a specific capacity of 775.0 mAh $g_{Zn}^{-1}$, which not only is significantly higher than the Pt/C + $RuO_2$ cell (668.4 mA h $g_{Zn}^{-1}$), but also approaches the theoretical capacity limit (823 mAh $g_{Zn}^{-1}$).[44] This feature reflects superior zinc utilization efficiency. Dynamic discharge measurements under varying current densities (1, 5, 10, and 20 mA $cm^{-2}$, Fig. 4d) further validate the operational stability and reversibility of the Fe/Ni-NC catalyst. Upon returning to a low current density (1 mA $cm^{-2}$), the discharge voltage is effectively restored to 1.36 V, compared to 1.34 V for the Pt/C + $RuO_2$-based cell.

Long-term cycling stability is important for the practical operation of rechargeable ZABs. As shown in Fig. 4e, the cell was subjected to repeated discharge–charge cycling at a current density of 10 mA $cm^{-2}$, with each cycle consisting of

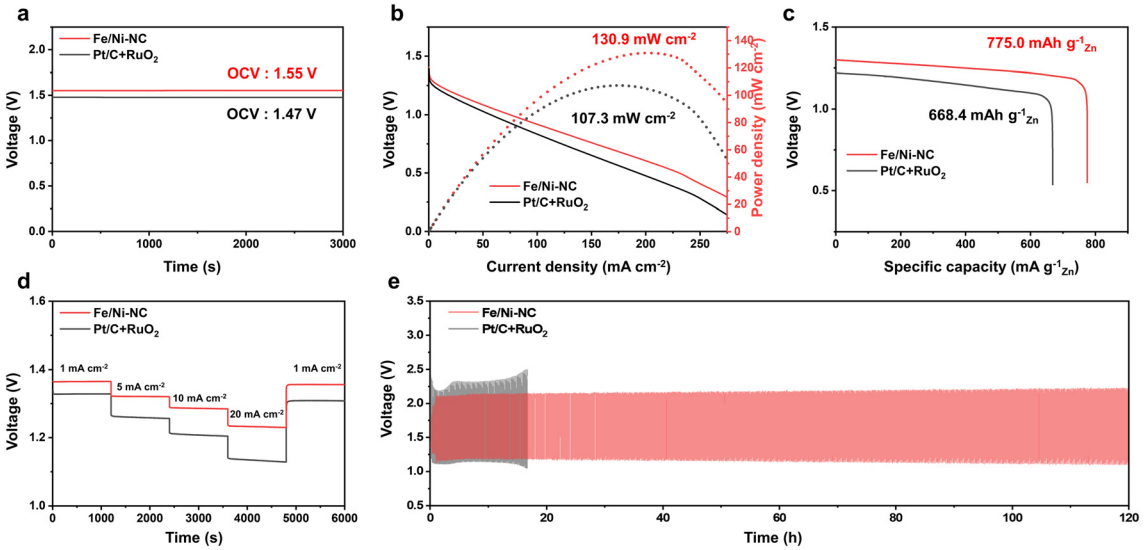


**Fig. 4** Zinc–air battery performance of Fe/Ni-NC (red) and Pt/C + $RuO_2$ (black) electrodes. (a) Open circuit voltage curves; (b) discharge polarization and power density curves; (c) galvanostatic full-discharge curves at a constant current density of 10 mA $cm^{-2}$; (d) galvanostatic discharge curves under different current densities; (e) long-term cycling performance at current density of 10 mA $cm^{-2}$.

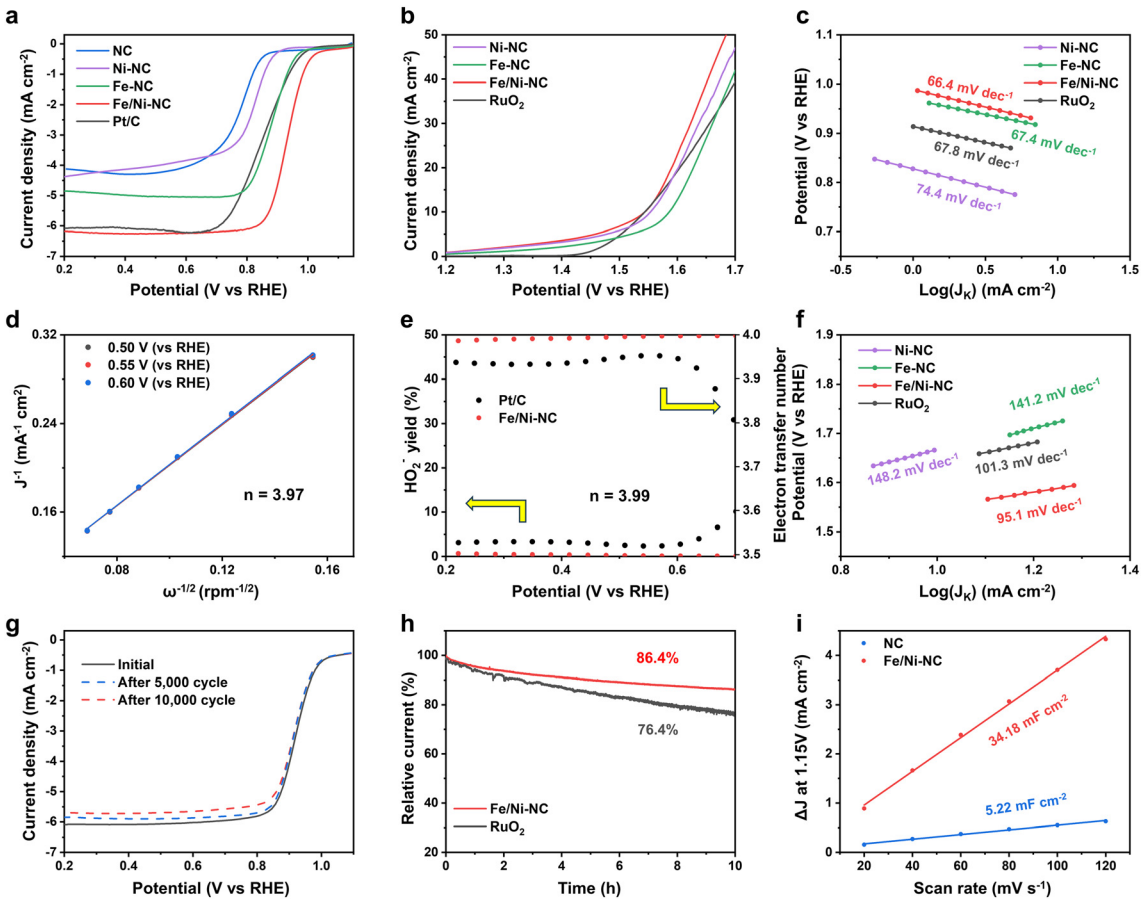


**Fig. 5** Electrocatalytic ORR and OER properties of Fe/Ni-NC and control samples. LSV polarization curves for (a) the ORR and (b) the OER; (c) Tafel plots under ORR measurement conditions; (d) Koutecký–Levich plot of Fe/Ni-NC at different potentials of 0.5–0.6 V *vs.* RHE; (e) electron transfer numbers and $HO_2^-$ yields of Fe/Ni-NC and Pt/C determined by RRDE measurements; (f) Tafel plots under OER measurement conditions; (g) ORR LSV polarization curves of Fe/Ni-NC at initial, 5000th, and 10 000th cycles; (h) CA curves of Fe/Ni-NC at a constant applied potential of 1.58 V *vs.* RHE; (i) capacitive current densities from NC and Fe/Ni-NC at different scan rates.

alternating 5 min discharge and charge periods. Under these conditions, the Fe/Ni-NC-based ZAB maintained a stable operating voltage for more than 120 h, corresponding to 720 continuous cycles. In contrast, the ZAB cell, assembled with Pt/C and $RuO_2$, stopped at 16 h (96 cycles). Additionally, STEM and EDS mapping images of the Fe/Ni-NC-after-cycle sample (Fig. S13) show almost no change in the carbon-network and the maintenance of atomically dispersed Fe-/Ni-containing species. These data reveal the excellent stability of Fe/Ni-NC materials under rigorous alkaline operation conditions of ZABs. Furthermore, comparison with previously reported rechargeable ZAB catalysts (Table S4) shows that the Fe/Ni-NC-based ZAB exhibits a competitive open-circuit potential and excellent long-term cycling stability.

Its outstanding activity, high energy output, and excellent stability, coupled with the use of earth-abundant Fe and Ni, firmly indicate that Fe/Ni-NC is a promising air cathode material for high-performance, cost-effective, and sustainable ZABs.

### 2.4 Electrochemical properties of Fe/Ni-NC

To elucidate the origin of the superior ZAB performance of Fe/Ni-NC, its bifunctional electrocatalytic activities toward the ORR and OER were investigated under half-cell conditions. The ORR activity was assessed by linear sweep voltammetry (LSV) using a rotating disk electrode (RDE) in $O_2$-saturated 0.1 M KOH electrolyte. The measurements were performed in a conventional three-electrode configuration at a scan rate of 5 mV $s^{-1}$ and a rotation speed of 1600 rpm. Fe/Ni-NC exhibits an onset potential of 1.03 V and a half-wave potential ($E_{1/2}$) of 0.93 V *vs.* the reversible hydrogen electrode (RHE), surpassing NC, Ni-NC, Fe-NC, and even the commercial Pt/C catalyst (Fig. 5a). The ORR response was further supported by additional CV measurements under $N_2$- and $O_2$-saturated conditions, in which cathodic peaks appeared only under $O_2$-saturated conditions (Fig. S14).[45] Such enhanced ORR activity of Fe/Ni-NC is attributed to the atomically dispersed metal–$N_x$ active sites embedded within the N-doped carbon matrix, which optimize the electronic environment and facilitate efficient adsorption and reduction of oxygen species. Furthermore, Fe/Ni-NC achieves a high limiting current density of 6.21 mA $cm^{-2}$, which could be associated with the hierarchical porous structure of Fe/Ni-NC, promoting mass transport and exposing accessible catalytic sites.[46] The OER performance was evaluated in $N_2$-saturated 1.0 M KOH electrolyte under the same experimental conditions. Fe/Ni-NC displays an overpotential of 320 mV at a current density of 10 mA $cm^{-2}$, which is lower than both Fe-NC and Ni-NC (Fig. 5b). Notably, this value is identical to the benchmark $RuO_2$ catalyst (320 mV), suggesting the excellent OER catalytic activity of Fe/Ni-NC.

Comparative analysis of the monometallic control samples reveals that Fe-NC exhibits moderately high ORR activity but lower OER performance, whereas Ni-NC displays improved OER performance yet poor ORR activity. The combined presence of Fe and Ni active sites provides a balanced contribution to both the ORR and OER, resulting in improved bifunctional activity compared to the monometallic catalysts.[47,48] This complementary behavior implies that the bifunctional performance of Fe/Ni-NC arises from the synergistic integration of Fe- and Ni-centered active sites. Importantly, the comparable BET surface areas of Fe/Ni-NC and the control samples further support the synergistic effect. In addition, the ORR/OER electrochemical data for Ni/Fe-NC prepared with the reversed doping sequence exhibit overall inferior electrocatalytic activities relative to Fe/Ni-NC (Fig. S15 and Table S3). This result indicates that the sequence of metal addition is important for the production process. These findings confirm that the rational design of dual-metal single-atom catalysts, including the active-site composition and production process, is crucial for optimizing bifunctional electrocatalytic performance, offering a promising strategy for advanced air electrode materials in metal–air batteries.[49,50]

Additional electrochemical analyses were carried out under ORR and OER operating conditions to understand electrochemical behaviors. Under ORR conditions, Fe/Ni-NC exhibits a Tafel slope of 66.4 mV $dec^{-1}$, comparable to that of commercial Pt/C (67.8 mV $dec^{-1}$), suggesting similar ORR reaction kinetics under the measured conditions (Fig. 5c). However, Fe/Ni-NC shows a more positive half-wave potential and a higher current density than Pt/C, indicating that its superior ORR performance arises not from a fundamentally different reaction pathway, but from the higher intrinsic activity of the active sites.[51] Electrochemical impedance spectroscopy (EIS) measurements at 0.85 V (*vs.* RHE) (Fig. S16) reveal the smallest semicircle diameter in the Nyquist plot for Fe/Ni-NC, suggesting the lowest charge transfer resistance ($R_{ct}$) among the catalysts tested and signifying enhanced electron transfer capability.[52] The Koutecký–Levich (K–L) plots (Fig. S17) recorded at various rotation speeds of polarization curves (400–2025 rpm) yield an average electron transfer number ($n$) of 3.97 (Fig. 5d),[53,54] implying a nearly complete four-electron reduction pathway. Complementary rotating ring-disk electrode (RRDE) measurements confirm these findings, showing a remarkably low $HO_2^-$ yield of 0.4% and a calculated $n$ value of 3.99, highlighting the superior selectivity of Fe/Ni-NC for the direct four-electron oxygen reduction pathway with minimal side reactions (Fig. 5e).

Under OER conditions in 1.0 M KOH, Fe/Ni-NC achieves a Tafel slope of 101 mV $dec^{-1}$, which is notably lower than Ni-NC (148 mV $dec^{-1}$) and Fe-NC (141 mV $dec^{-1}$) (Fig. 5f). These results indicate significantly improved reaction kinetics for oxygen evolution.[55] EIS measurements at 1.64 V (*vs.* RHE) (Fig. S16) reveal that Fe/Ni-NC exhibits a Nyquist semicircle diameter comparable to that of $RuO_2$, indicating that its transfer resistance ($R_{ct}$) is similarly low. Notably, Fe/Ni-NC shows smaller semicircle diameters compared to NC, confirming significantly enhanced charge transport during the OER process.

Table S3 summarizes the key electrocatalytic ORR and OER parameters of Fe/Ni-NC, noble-metal reference catalysts, and monometallic control samples. To quantify the bifunctional catalytic performance, the potential gap ($\Delta E$) is commonly utilized as a key metric, representing the numerical difference between the potential required to achieve a current density of 10 mA $cm^{-2}$ for the OER and the half-wave potential ($E_{1/2}$) for the ORR. A lower $\Delta E$ value reflects enhanced bifunctional catalytic activity and is therefore regarded as an important performance metric for rechargeable ZABs. Fe/Ni-NC exhibits a significantly smaller $\Delta E$ compared to both the noble-metal benchmark (Pt/C and $RuO_2$) (Fig. S18) and the monometallic catalysts (Fe-NC and Ni-NC), highlighting the synergistic effect of the dual-metal SAC structure in operating both ORR and OER processes (see below for further discussion). Additionally, Fig. S18 and Table S4 present a comparison of $\Delta E$ values from previously reported Fe- or Ni-based electrocatalytic systems. Among them, Fe/Ni-NC shows the lowest value, further emphasizing its excellent bifunctional catalytic efficiency and strong potential as a cost-effective alternative to noble-metal-based air cathode materials.

The long-term durability of Fe/Ni-NC was assessed by cyclic voltammetry (CV) and chronoamperometric (CA) measurements for the ORR and OER, respectively. CV measurements were performed at a scan rate of 100 mV $s^{-1}$, and LSV measurements were performed at a scan rate of 5 mV $s^{-1}$ after the 5000 and 10 000 cycles (Fig. 5g). The half-wave potential of Fe/Ni-NC barely decreased. CA was performed at 1.58 V (*vs.* RHE) over 10 hours (Fig. 5h). The catalyst retained 86.4% of its initial current density, demonstrating excellent electrochemical stability. In contrast, the current density of $RuO_2$ decreased dramatically, retaining only 76.4% of its initial value. Such remarkable half-cell stability is reflected in the long-term durability of the Fe/Ni-NC-based ZAB.

The electrochemically active surface area (ECSA) was estimated from the double-layer capacitance ($C_{dl}$) obtained in the non-faradaic region of cyclic voltammograms in $N_2$-saturated 0.1 M KOH (Fig. 5i). Fe/Ni-NC displays a significantly larger $C_{dl}$ of 34.14 mF $cm^{-2}$ compared to NC (5.22 mF $cm^{-2}$), suggesting a much higher density of electroactive sites, attributed to the incorporation of atomically dispersed Fe and Ni centers and improved catalyst utilization. All the electrochemical characterization results discussed in this section support the excellent electrocatalytic properties of Fe/Ni-NC.

### 2.5 DFT for electrocatalytic bifunctional activity of Fe/Ni-NC

To elucidate the origin of the superior bifunctional OER/ORR activity in Fe/Ni-NC structures, we performed density functional theory (DFT) calculations exploring the reaction mechanisms and structural stability. Based on the XPS results, which identified pyridinic (PdN) and pyrrolic (PrN) nitrogen as the dominant nitrogen species in the catalyst, we constructed the corresponding N-doped carbon models as representative local coordination environments for the DFT calculations. These structural motifs have also been widely used in previous theoretical studies as representative models for pyridinic- and pyrrolic-N environments in M–N–C catalysts.[56–58] Fe-NC and Ni-NC structures were modeled by embedding Fe or Ni atoms into the defects, yielding Fe-doped pyridinic (Fe@PdN), Ni-doped pyridinic (Ni@PdN), Fe-doped pyrrolic (Fe@PrN) and Ni-doped pyrrolic (Ni@PrN) configurations. Additionally, large NC supercells containing either a pyridinic or a pyrrolic defect, each co-doped with both Fe and Ni, were constructed to model the structure of Fe/Ni-NC (mPdN and mPrN). The construction leads to 6 structures as shown in Fig. S19. As shown in Fig. S20, the analysis of metal binding energy indicates a slight thermodynamic preference for PdN defects compared to PrN defects. Additionally, the negative binding energy values confirm that the incorporation of Fe and Ni into both defect types is thermodynamically favorable.

Based on the designed structures, the OER and ORR reaction mechanisms were investigated by calculating the adsorption free energies of the reaction intermediates and analyzing the corresponding free energy diagrams (FEDs). For the adsorption studies on the Fe/Ni-NC structures, four configurations including Ni@mPdN, Ni@mPrN, Fe@mPdN, and Fe@mPrN were examined based on the two structures (mPrN and mPdN), where Ni and Fe denote the active sites. Detailed FEDs for all structures are presented in Fig. S21. In general, the Fe sites exhibit stronger adsorption toward the adsorbates than the Ni sites for both types of defects, and the Ni active sites in the PrN environment show significantly stronger adsorption than the Ni sites in the PdN structures. Although various active sites coexist on the catalyst surface, the adsorbates first occupy the sites with the lowest adsorption free energies, while the electrochemical reaction proceeds most readily at the sites that require the lowest overpotentials. Therefore, to enable a clearer comparison, the reaction pathways with the smallest $\eta_{OER}$ and $\eta_{ORR}$ for the Fe-NC, Ni-NC, and Fe/Ni-NC systems were extracted and plotted in Fig. 6a and b, respectively. Notably, the DFT-calculated OER/ORR activities show excellent consistency with the experimental trends (Fe/Ni-NC > Ni-NC > Fe-NC for the OER and Fe/Ni-NC > Fe-NC > Ni-NC for the ORR).

For the OER, the Ni site in the FeNi@mPrN structure (Ni@mPrN) exhibits the highest catalytic activity with $\eta_{OER}$ = 0.43 V, which is very close to that of the Ni site in the Ni@PrN structure ($\eta_{OER}$ = 0.45 V). In contrast, the Fe site in the Fe@PrN structure shows poor OER performance with $\eta_{OER}$ = 0.67 V. The superior OER activity of Ni@mPrN structure arises from its weakened O* adsorption, which shifts the potential-determining step (PDS) from O* → OOH* to the more favorable OH* → O* step requiring a lower overpotential. For the ORR, Ni@mPrN also exhibits superior catalytic activity with $\eta_{ORR}$ = 0.53 V, outperforming Fe@PdN (0.66 V) and Ni@PrN (0.84 V). This enhanced performance stems from its weaker interaction with the O*

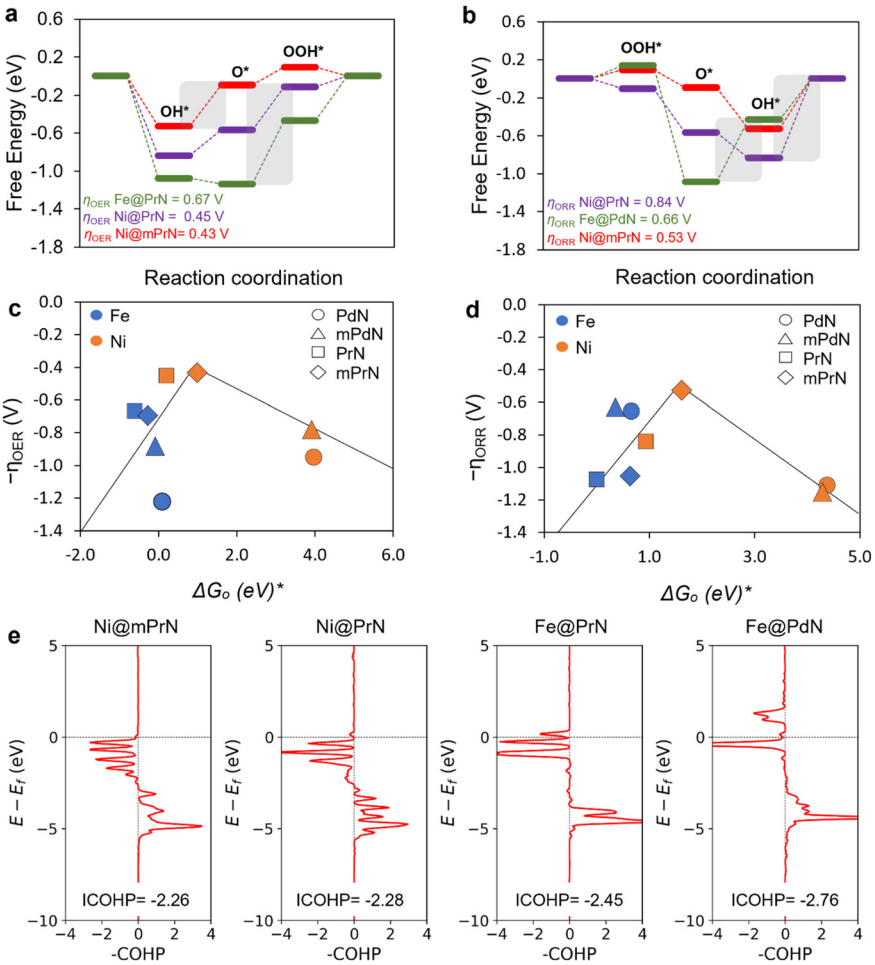


**Fig. 6** Free energy diagram of the (a) OER and (b) ORR pathways under ideal alkaline conditions for the Fe-NC, Ni-NC, and Fe/Ni-NC structures exhibiting the lowest OER overpotential ($\eta_{OER}$) and ORR overpotential ($\eta_{ORR}$); volcano plot of (c) $\eta_{OER}$ and (d) $\eta_{ORR}$ *versus* Gibbs free energy of O* adsorption ($\Delta G_{O*}$) for all designed structures; (e) COHP analysis of the O* bonding strength for the structures in Fig. 6a and b. The bond strength is quantified by the integrated COHP (ICOHP) values up to the Fermi level.

intermediate: while Fe@PdN and Ni@PrN bind O* too strongly, Ni@mPrN shows significantly lower adsorption free energy for the O* intermediate. The volcano plots in Fig. 6c and d illustrate the correlation between $\eta_{OER}$, $\eta_{ORR}$, and the adsorption free energy of O* ($\Delta G_{O*}$). The analysis identifies that Ni@PdN and Ni@mPdN bind O* too weakly, whereas Fe@PrN and Fe@mPrN bind it too strongly, positioning both far from the Sabatier optimum. Doping Ni into PrN defects significantly strengthens O* binding on Ni@PrN and Ni@mPrN, while doping Fe into PdN defects slightly weakens O* binding on Fe@PdN and Fe@mPdN. Among these structures, Ni@mPrN achieves an optimal $\Delta G_{O*}$ in both volcano plots, thereby exhibiting bifunctional activity for both the OER and ORR.

Electronic structure analysis provides a compelling explanation for the varying O* binding strengths observed across the structures in the volcano plots. Fig. S22 and S23 present the density of states (DOS) for all structures and the d-band centers at the Fe and Ni active sites, respectively. The d-band center positions of Fe and Ni sites exhibit marked variations depending on whether they are coordinated to PdN or PrN defects. Specifically, Ni doping into PrN defects (Ni@PrN) shifts the Ni d-band center upward compared to PdN environments (Ni@PdN), whereas the Fe@PrN d-band center shifts downward relative to Fe@PdN. Consistent with experimental ORR measurements showing the superior activity of Fe/Ni-NC over Fe-NC, our calculations attribute this enhancement to the emergence of Ni@mPrN sites, which are uniquely formed in Fe/Ni-NC and serve as the dominant ORR active centers. Thus, Ni@mPrN exhibits bifunctional behavior, efficiently catalyzing both the OER and ORR. This unique performance arises from the synergistic interplay of three factors: electronic structure, adsorption geometry, and O* binding strength. To further substantiate this interpretation, we performed a detailed electronic structure analysis, including d-band center shifts (Fig. S23) and optimized O adsorption geometries (Fig. S24), which collectively rationalize the weakened O binding and enhanced catalytic response of Ni@mPrN (see SI for further discussion).

Previous studies have shown that changes in the adsorption geometry can disrupt scaling relations, leading to weaker reaction kinetic and enhanced catalytic activity.[59] To probe O* binding strengths across active sites further, O* intermediate bond strengths were quantified *via* ICOHP for the structures in Fig. 6a and b. As revealed by the ICOHP analysis in Fig. 6e, the occupation of strong antibonding states near the Fermi level for Ni@mPrN destabilizes the adsorbate–surface interaction, leading to a notable reduction in O* binding strength. Therefore, Ni@mPrN exhibits slightly weaker O* binding (more positive ICOHP value) than Ni@PrN and significantly weaker binding than Fe@PdN or Fe@PrN, consistent with the aforementioned O* adsorption trends. Overall, the computational findings demonstrate that Ni@mPrN optimally balances electronic structure and O* binding strength, establishing it as the dominant bifunctional OER/ORR active site in Fe/Ni-NC and underscoring the exceptional bifunctional catalytic activity observed experimentally.

# 3 Conclusions

In this work, we successfully developed a bimetallic SAC catalyst (Fe/Ni-NC) by sequentially anchoring Fe and Ni species on nitrogen-doped porous carbon derived from ZIF-8. Structural characterization, including XANES and EXAFS, revealed that both Fe and Ni atoms are atomically dispersed and coordinated with nitrogen species without forming metallic or oxide particles. The resulting Fe/Ni-NC catalyst exhibits a high surface area, hierarchical porous structure, and uniformly distributed active sites, which collectively contribute to its outstanding bifunctional electrocatalytic performance.

When utilized as an air cathode for rechargeable ZABs, Fe/Ni-NC not only achieved a high OCV of 1.55 V and a peak power density of 130.9 mW $cm^{-2}$ but also delivered a specific capacity 775.0 mAh $g_{Zn}^{-1}$ nearing the theoretical maximum. These battery metrics are complemented by superior bifunctional kinetics for the ORR and OER, as evidenced by its high selectivity and low charge transfer resistance, which collectively enable a remarkable cycling lifespan of over 120 h. Such performance highlights the catalyst's clear advantage over the noble-metal Pt/C + $RuO_2$ benchmark. Complementary DFT analysis provides mechanistic insight into these experimental observations by identifying Ni sites embedded within pyrrolic-N environments (Ni@mPrN) as the dominant active configurations responsible for the enhanced bifunctional activity. Theoretical results show that these sites possess optimal O* adsorption energetics and favorable electronic structures, which rationalize the synergistic interaction between Fe and Ni single atoms within the N-doped carbon matrix. Its electrochemical behavior not only outperforms those of monometallic counterparts and commercial Pt/C and $RuO_2$ catalysts, but also strongly supports the synergistic effect derived from the bioinspired dual-metal single-atom-based active species on the surfaces of carbon-based porous networks. These features collectively validate the potential of Fe/Ni-NC as a next-generation bifunctional electrocatalyst for advanced metal–air energy systems.

# 4 Experimental section

### 4.1 Preparation of NC

The synthesis of N-doped porous carbon (NC) began with the preparation of ZIF-8 precursors. In a typical procedure, 4016 mg of zinc nitrate hexahydrate and 4926 mg of 2-methylimidazole were individually dissolved in 115 mL and 110 mL of methanol, respectively. These solutions were mixed in a 250 mL round-bottom flask and subjected to continuous stirring for 24 h. The resulting white precipitates were isolated by centrifugation, washed with methanol three times, and subsequently dried under vacuum at 60 °C. To obtain the carbonized framework, the dried ZIF-8 was placed in an alumina crucible and positioned at the center of a quartz tube furnace. Thermal treatment was conducted by ramping the temperature to 950 °C (5 °C $min^{-1}$) and maintaining this temperature for 3 h under a steady stream of $N_2$. After the furnace naturally cooled to room temperature, 350 mg of the carbonized powder was dispersed in 100 mL of 1 M HCl and sonicated at 80 °C for 5 h to remove residual zinc and other contaminants. The purified sample was recovered through membrane filtration (Model H020A047A, Advantech Corp.), washed with ethanol and deionized water, and dried at 60 °C for 12 h to yield the final NC product (320 mg).

### 4.2 Electrochemical properties of Fe/Ni-NC

The bimetallic Fe/Ni-NC was fabricated through a sequential metal-coordination method. First, 100 mg of NC was dispersed in 50 mL of ethylene glycol (EG) by sonication for 30 min. Separately, 0.5 mmol iron(II) chloride tetrahydrate was dissolved in 50 mL of EG. These two mixtures were combined and stirred at 180 °C for 5 h. The Fe-anchored intermediates were filtered, washed with EG, deionized water, and ethanol, and dried at 60 °C for 12 h. This procedure was repeated for Ni incorporation by reacting 100 mg of the Fe-pre-treated powder with 0.5 mmol of nickel(II) chloride hexahydrate in EG under the same conditions (180 °C for 5 h). Following filtration, washing, and drying, the resulting bimetallic precursor was placed in an alumina crucible and positioned at the center of a quartz tube furnace. Thermal treatment was conducted by ramping the temperature to 900 °C (5 °C $min^{-1}$) and maintaining this temperature for 1 h under a steady stream of $N_2$. Finally, after the furnace naturally cooled to room temperature, the Fe/Ni-NC product (98 mg) was obtained.

# Author contributions

Sunggu Park: writing – original draft, methodology, investigation, formal analysis, data curation, and

conceptualization. Hung Ngo Manh: writing – original draft, investigation, formal analysis, and data curation. Seyeop Jeong: writing – original draft, methodology, investigation, formal analysis, data curation, and conceptualization. Heesun Kim: resources. Jun Ho Seok: data curation. Seokhyeon Jeon and Yunseok Shin: conceptualization. Ali Anus: writing – review & editing. Sang Uck Lee, and Sungjin Park: writing – review & editing, validation, supervision, project administration, funding acquisition, and conceptualization.

## Conflicts of interest

The authors declare no conflict of interest.

## Data availability

The data supporting this article have been included as part of the supplementary information (SI).

Supplementary information: additional experimental methods and results are available online. See DOI: https://doi.org/10.1039/d6im00077k.

## Acknowledgements

This work was supported by the National Research Foundation of Korea (NRF) grants funded by the Korean government (MSIT) (RS-2024-00335043 and RS-2024-00415940). We thank the Busan Center at the Korea Basic Science Institute (KBSI) for XPS analysis. X-ray absorption spectroscopy (XAS) measurements were conducted using the beamline 10C at the Pohang Accelerator Laboratory (PAL, Pohang, South Korea).

## References

1 Y. Chen, J. Xu, P. He, Y. Qiao, S. Guo, H. Yang and H. Zhou, Metal-air batteries: Progress and perspective, *Sci. Bull.*, 2022, **67**, 2449–2486.
2 F. Cheng and J. Chen, Metal-air batteries: From oxygen reduction electrochemistry to cathode catalysts, *Chem. Soc. Rev.*, 2012, **41**, 2172–2192.
3 A. Iqbal, O. M. El-Kadri and N. M. Hamdan, Insights into rechargeable Zn-air batteries for future advancements in energy storing technology, *J. Energy Storage*, 2023, **62**, 106926.
4 A. I. Douka, H. Yang, L. Huang, S. Zaman, T. Yue, W. Guo, B. You and B. Y. Xia, Transition metal/carbon hybrids for oxygen electrocatalysis in rechargeable zinc-air batteries, *EcoMat*, 2021, **3**, e12067.
5 S. Ren, X. Duan, S. Liang, M. Zhang and H. Zheng, Bifunctional electrocatalysts for Zn-air batteries: Recent developments and future perspectives, *J. Mater. Chem. A*, 2020, **8**, 6144–6182.
6 G. C. da Silva, M. R. Fernandes and E. A. Ticianelli, Activity and stability of Pt/$IrO_2$ bifunctional materials as catalysts for the oxygen evolution/reduction reactions, *ACS Catal.*, 2018, **8**, 2081–2092.
7 G. Park, M. Kim, J. Y. Park and K. M. Nam, Addressing selectivity challenges in seawater splitting: Catalyst design for oxygen and chlorine evolution reactions, *Bull. Korean Chem. Soc.*, 2025, **46**, 253–264.
8 H. Seong and D. Lee, Atomically precise metal nanoclusters for energy conversion, *Bull. Korean Chem. Soc.*, 2024, **45**, 435–450.
9 B. A. Brandes, Y. Krishnan, F. L. Buchauer, H. A. Hansen and J. Hjelm, Unifying the ORR and OER with surface oxygen and extracting their intrinsic activities on platinum, *Nat. Commun.*, 2024, **15**, 7336.
10 R. Qin, G. Chen, X. Feng, J. Weng and Y. Han, Ru/Ir-based electrocatalysts for oxygen evolution reaction in acidic conditions: From mechanisms, optimizations to challenges, *Adv. Sci.*, 2024, **11**, 2309364.
11 Z. Wang, C. Zhu, H. Tan, J. Liu, L. Xu, Y. Zhang, Y. Liu, X. Zou, Z. Liu and X. Lu, Understanding the synergistic effects of cobalt single atoms and small nanoparticles: Enhancing oxygen reduction reaction catalytic activity and stability for zinc-air batteries, *Adv. Funct. Mater.*, 2021, **31**, 2104735.
12 X. Zhuo, W. Jiang, G. Qian, J. Chen, T. Yu, L. Luo, L. Lu, Y. Chen and S. Yin, $Ni_3S_2$/Ni heterostructure nanobelt arrays as bifunctional catalysts for urea-rich wastewater degradation, *ACS Appl. Mater. Interfaces*, 2021, **13**, 35709–35718.
13 R. Li, P. Rao, D. Wu, J. Li, P. Deng, Z. Miao and X. Tian, Understanding the bifunctional trends of Fe-based binary single-atom catalysts, *Adv. Sci.*, 2023, **10**, 2301566.
14 J. Kim, O. Gwon, O. Kwon, J. Mahmood, C. Kim, Y. Yang, H. Lee, J. H. Lee, H. Y. Jeong and J.-B. Baek, Synergistic coupling derived cobalt oxide with nitrogenated holey two-dimensional matrix as an efficient bifunctional catalyst for metal-air batteries, *ACS Nano*, 2019, **13**, 5502–5512.
15 H. Shin, S. Geum, J. Lee, M. Shin, K. M. Ok, S. J. Kwon and J. Do, Comparison of oxygen evolution reaction performance for Ni and Co using isostructural trans-cinnamate complexes, *Bull. Korean Chem. Soc.*, 2024, **45**, 920–928.
16 W. Xu, Y. Wu, W. Gu, D. Du, Y. Lin and C. Zhu, Atomic-level design of metalloenzyme-like active pockets in metal-organic frameworks for bioinspired catalysis, *Chem. Soc. Rev.*, 2024, **53**, 137–162.
17 J. Barrio, A. Pedersen, S. Favero, H. Luo, M. Wang, S. C. Sarma, J. Feng, L. T. T. Ngoc, S. Kellner and A. Y. Li, Bioinspired and bioderived aqueous electrocatalysis, *Chem. Rev.*, 2022, **123**, 2311–2348.
18 J. Chen, H. Li, C. Fan, Q. Meng, Y. Tang, X. Qiu, G. Fu and T. Ma, Dual single-atomic Ni-$N_4$ and Fe-$N_4$ sites constructing Janus hollow graphene for selective oxygen electrocatalysis, *Adv. Mater.*, 2020, **32**, 2003134.
19 F. Luo, J. Zhu, S. Ma, M. Li, R. Xu, Q. Zhang, Z. Yang, K. Qu, W. Cai and Z. Chen, Regulated coordination environment of Ni single atom catalyst toward high-efficiency oxygen electrocatalysis for rechargeable zinc-air batteries, *Energy Storage Mater.*, 2021, **35**, 723–730.
20 J. H. Kim and S. H. Joo, Rise of atomically dispersed metal catalysts: Are they a new class of catalysts?, *Bull. Korean Chem. Soc.*, 2024, **45**, 350–358.

21 Z. Chen, W. Cheng, K. Cao, M. Jin, S. Rahali, S. A. Chala, E. Ebrahimi, N. Ma, R. Liu and K. Lakshmanan, A bifunctional iron-nickel oxygen reduction/oxygen evolution catalyst for high-performance rechargeable zinc-air batteries, *Small*, 2025, **21**, 2409161.
22 Y. Zhong, X. Xu, W. Wang and Z. Shao, Recent advances in metal-organic framework derivatives as oxygen catalysts for zinc-air batteries, *Batteries Supercaps*, 2019, **2**, 272–289.
23 G. Huang, M. Ren, Y. Wang, J. Zhou and J. Cai, Direct carbonization of ZIF-8 to N-doped carbons: Amino acid modulation and enhanced catalytic activity for oxygen reduction reaction, *Mater. Chem. Phys.*, 2019, **237**, 121856.
24 Y. Wang, J. Wang, X. Feng, G. Chen, X. Wang, T. Gan, X. Fan, H. Lin and Y. Han, Synergistic Fe-Ni dual-atom sites on hollow carbon enabling high-performance rechargeable zinc-air batteries, *Chem. Sci.*, 2026, **17**, 2155–2163.
25 S. Ren, X. Tang, P. Zhang, W. Peng, X. Zeng, H. Zheng and Z. Wan, Multi-scale porous nitrogen-rich large carbon networks modified by bimetallic FeNi alloys as exceptional bifunctional catalysts for rechargeable Zn-air batteries, *J. Energy Storage*, 2025, **105**, 114740.
26 Y.-R. Lee, M.-S. Jang, H.-Y. Cho, H.-J. Kwon, S. Kim and W.-S. Ahn, ZIF-8: A comparison of synthesis methods, *Chem. Eng. J.*, 2015, **271**, 276–280.
27 J. Dai, J. Zhang, R. Karthick, M. Liang, Q. Wei, X. Chen, Y. Shi, S. Zhai, G. Wang and F. Chen, Co/$Fe_3O_4$ nanoparticles embedded in N-doped hierarchical porous carbon derived from zeolitic imidazolate frameworks as efficient oxygen reduction electrocatalysts for zinc-air battery-based desalination, *J. Mater. Chem. A*, 2022, **10**, 12213–12224.
28 C. Jia, Y. Zhao, S. Song, Q. Sun, Q. Meyer, S. Liu, Y. Shen and C. Zhao, Highly ordered hierarchical porous single-atom Fe catalyst with promoted mass transfer for efficient electroreduction of $CO_2$, *Adv. Energy Mater.*, 2023, **13**, 2302007.
29 A. C. Ferrari and J. Robertson, Interpretation of Raman spectra of disordered and amorphous carbon, *Phys. Rev. B: Condens. Matter Mater. Phys.*, 2000, **61**, 14095–14107.
30 M. Thommes, K. Kaneko, A. V. Neimark, J. P. Olivier, F. Rodriguez-Reinoso, J. Rouquerol and K. S. W. Sing, Physisorption of gases, with special reference to the evaluation of surface area and pore size distribution (IUPAC Technical Report), *Pure Appl. Chem.*, 2015, **87**, 1051–1069.
31 Y. Fang, D. Gu, Y. Zou, Z. Wu, F. Li, R. Che, Y. Deng, B. Tu and D. Zhao, A low-concentration hydrothermal synthesis of biocompatible ordered mesoporous carbon nanospheres with tunable and uniform size, *Angew. Chem., Int. Ed.*, 2010, **49**, 7987–7991.
32 J. C. Groen, L. A. A. Peffer and J. Pérez-Ramírez, Pore size determination in modified micro- and mesoporous materials: Pitfalls and limitations in gas adsorption data analysis, *Microporous Mesoporous Mater.*, 2003, **60**, 1–17.
33 R. Wu, Z. Zhang, B. Yu and Z. Chen, One-step pyrolysis of ZIF-8 after recovering rare earth elements from mining wastewater as a functional Fenton-like catalyst, *Chem. Eng. J.*, 2024, **502**, 158122.
34 Y. Deng, J. Pang, W. Ge, M. Zhang, W. Zhang, W. Zhang, M. Xiang, Q. Zhou and J. Bai, Constructing atomically dispersed Mn on ZIF-derived nitrogen-doped carbon for boosting oxygen reduction, *Front. Chem.*, 2022, **10**, 969905.
35 J. Xiong, X. Chen, Y. Zhang, Y. Lu, X. Liu, Y. Zheng, Y. Zhang and J. Lin, Fe/Co/N-C/graphene derived from Fe/ZIF-67/graphene oxide three dimensional frameworks as a remarkably efficient and stable catalyst for the oxygen reduction reaction, *RSC Adv.*, 2022, **12**, 2425–2435.
36 W. Ju, A. Bagger, G.-P. Hao, A. S. Varela, I. Sinev, V. Bon, B. Roldan Cuenya, S. Kaskel, J. Rossmeisl and P. Strasser, Understanding activity and selectivity of metal-nitrogen-doped carbon catalysts for electrochemical reduction of $CO_2$, *Nat. Commun.*, 2017, **8**, 944.
37 Y. Wen, C. Ma, Z. Wei, X. Zhu and Z. Li, FeNC/MXene hybrid nanosheet as an efficient electrocatalyst for oxygen reduction reaction, *RSC Adv.*, 2019, **9**, 13424–13430.
38 R. Boppella, M. Austeria P, Y. Kim, E. Kim, I. Song, Y. Eom, D. P. Kumar, M. Balamurugan, E. Sim and D. H. Kim, Pyrrolic N-stabilized monovalent Ni single-atom electrocatalyst for efficient $CO_2$ reduction: Identifying the role of pyrrolic-N and synergistic electrocatalysis, *Adv. Funct. Mater.*, 2022, **32**, 2202351.
39 T. E. Westre, P. Kennepohl, J. G. DeWitt, B. Hedman, K. O. Hodgson and E. I. Solomon, A multiplet analysis of Fe K-edge 1s→3d pre-edge features of iron complexes, *J. Am. Chem. Soc.*, 1997, **119**, 6297–6314.
40 T. Marshall-Roth, N. J. Libretto, A. T. Wrobel, K. J. Anderton, M. L. Pegis, N. D. Ricke, T. Van Voorhis, J. T. Miller and Y. Surendranath, A pyridinic Fe-$N_4$ macrocycle models the active sites in Fe/N-doped carbon electrocatalysts, *Nat. Commun.*, 2020, **11**, 5283.
41 M. Akri, S. Zhao, X. Li, K. Zang, A. F. Lee, M. A. Isaacs, W. Xi, Y. Gangarajula, J. Luo and Y. Ren, Atomically dispersed nickel as coke-resistant active sites for methane dry reforming, *Nat. Commun.*, 2019, **10**, 5181.
42 P. Peng, L. Shi, F. Huo, C. Mi, X. Wu, S. Zhang and Z. Xiang, A pyrolysis-free path toward superiorly catalytic nitrogen-coordinated single atom, *Sci. Adv.*, 2019, **5**, eaaw2322.
43 W. Qu, J. Zhu, G. Cao, S. Chen, Y. Tan, B. Chen and M. Zhang, Ni single-atom dual catalytic electrodes for long life and high energy efficiency zinc-iodine batteries, *Small*, 2024, **20**, 2310475.
44 D. Kundu, B. D. Adams, V. Duffort, S. H. Vajargah and L. F. Nazar, A high-capacity and long-life aqueous rechargeable zinc battery using a metal oxide intercalation cathode, *Nat. Energy*, 2016, **1**, 16119.
45 L. An, Z. Zhang, J. Feng, F. Lv, Y. Li, R. Wang, M. Lu, R. B. Gupta, P. Xi and S. Zhang, Heterostructure-promoted oxygen electrocatalysis enables rechargeable zinc-air battery with neutral aqueous electrolyte, *J. Am. Chem. Soc.*, 2018, **140**, 17624–17631.
46 Q. Jing, Z. Mei, X. Sheng, X. Zou, Y. Yang, C. Zhang, L. Wang, Y. Sun, L. Duan and H. Guo, 3d orbital electron engineering in oxygen electrocatalyst for zinc-air batteries, *Chem. Eng. J.*, 2023, **462**, 142321.

47 Y. Wang, J. Wu, S. Tang, J. Yang, C. Ye, J. Chen, Y. Lei and D. Wang, Synergistic Fe-Se atom pairs as bifunctional oxygen electrocatalysts boost low-temperature rechargeable Zn-air battery, *Angew. Chem., Int. Ed.*, 2023, **62**, e202219191.
48 Y. Song, W. Li, K. Zhang, C. Han and A. Pan, Progress on bifunctional carbon-based electrocatalysts for rechargeable zinc-air batteries based on voltage difference performance, *Adv. Energy Mater.*, 2024, **14**, 2303352.
49 H. Liu, F. Yu, K. Wu, G. Xu, C. Wu, H. K. Liu and S. X. Dou, Recent progress on Fe-based single/dual-atom catalysts for Zn-air batteries, *Small*, 2022, **18**, 2106635.
50 Y. Wu, C. Ye, L. Yu, Y. Liu, J. Huang, J. Bi, L. Xue, J. Sun, J. Yang and W. Zhang, Soft template-directed interlayer confinement synthesis of a Fe-Co dual single-atom catalyst for Zn-air batteries, *Energy Storage Mater.*, 2022, **45**, 805–813.
51 Y. Shin, Y. Lee, C. Jo, Y. H. Kim and S. Park, $Co(O)_4(N)$-type single-atom-based catalysts and ligand-driven modulation of electrocatalytic properties for reducing oxygen molecules, *EcoEnergy*, 2024, **2**, 154–168.
52 J. Diao, Y. Qiu, S. Liu, W. Wang, K. Chen, H. Li, W. Yuan, Y. Qu and X. Guo, Interfacial engineering of $W_2N$/WC heterostructures derived from solid-state synthesis: A highly efficient trifunctional electrocatalyst for ORR, OER, and HER, *Adv. Mater.*, 2020, **32**, 1905679.
53 M. Jahan, Q. Bao and K. P. Loh, Electrocatalytically active graphene-porphyrin MOF composite for oxygen reduction reaction, *J. Am. Chem. Soc.*, 2012, **134**, 6707–6713.
54 P. K. Sonkar, K. Prakash, M. Yadav, V. Ganesan, M. Sankar, R. Gupta and D. K. Yadav, Co(II)-porphyrin-decorated carbon nanotubes as catalysts for oxygen reduction reactions: An approach for fuel cell improvement, *J. Mater. Chem. A*, 2017, **5**, 6263–6276.
55 T. Shinagawa, A. T. Garcia-Esparza and K. Takanabe, Insight on Tafel slopes from a microkinetic analysis of aqueous electrocatalysis for energy conversion, *Sci. Rep.*, 2015, **5**, 13801.
56 J. Park, J. Park, J. H. Seok, J. S. Byun, C. Oh, E. D. Kim, Y. J. Ko, Y. Kim, G. Sim and M. J. Kim, Modulation of electronic structure in Kraft lignin-derived Mo single-atom catalysts for optimized electrochemical oxygen reduction, *Adv. Sci.*, 2026, **13**, e22273.
57 K. Bhunia, J. H. Seok, M. Perumalsamy, K. S. Bejigo, V. Elumalai, S. U. Lee and S.-J. Kim, Atomically dispersed dual iron and manganese anchored nitrogen doped reduced graphene as robust cathode catalyst for direct methanol fuel cell and aluminium air battery, *Nano Energy*, 2024, **129**, 109966.
58 W. Guo, M. Pan, Q. Xie, H. Fan, L. Luo, Q. Jing, Y. Shen, Y. Yan, M. Liu and Z. Wang, Achieving pH-universal oxygen electrolysis via synergistic density and coordination tuning over biomass-derived Fe single-atom catalyst, *Nat. Commun.*, 2025, **16**, 2920.
59 D. Zhang, F. She, J. Chen, L. Wei and H. Li, Why do weak-binding M-N-C single-atom catalysts possess anomalously high oxygen reduction activity?, *J. Am. Chem. Soc.*, 2025, **147**, 6076–6086.